The Structure of Triple Flames Stabilized on a Slot Burner

RICCARDO AZZONI, STEFANO RATTI, SURESH K. AGGARWAL, and ISHWAR K. PURI*

Department of Mechanical Engineering (M/C 251), University of Illinois at Chicago, 842 W. Taylor St., Rm. 2039, Chicago, IL 60607-7022

A triple flame is a partially premixed flame that contains two premixed reaction zones (one fuel-lean and the other rich) that form exterior wings and a nonpremixed reaction zone that is established in between these wings. The three reaction zones merge at a "triple point." Triple flames may play an important role in the stabilization and liftoff of laminar nonpremixed flames. They are also of fundamental importance in the reignition of turbulent mixtures. Despite their importance, many aspects of triple flames have not been adequately investigated and are, consequently, not clearly understood. Herein, laminar triple flames stabilized on a Wolfhard-Parker slot burner are investigated. The flow consists of a rich mixture of methane and air emerging from the inner slot and a lean mixture from two symmetric outer slots. In this configuration the three reaction zones that characterize a triple flame can be clearly distinguished. The loci of the "triple points" form a "triple line" in this planar configuration. The velocity field is characterized using laser Doppler velocimetry, and the temperature distribution using laser interferometric holography. In addition, C_2^*-chemiluminescence images of the three reaction zones are obtained. A detailed numerical model is employed to completely characterize the flame. It is based on a 24-species and 81-reaction mechanism. The numerical results are validated through comparisons with the experimental measurements. Our results focus on the detailed structure, the interaction between the three reaction zones, the dependence of the flame structure on the initial velocities and mixture equivalence ratios, and the dominant chemical pathways. The lean premixed reaction zone (external wing) exhibits different features from the rich premixed reaction zone. In particular, it is characterized by strong HO_2 formation and consumption reactions, and by relatively weak methane consumption reactions. Radical activity is higher in the nonpremixed reaction zone than in the other reaction zones. Overall, radicals from the nonpremixed reaction zone are transported to both the rich and lean premixed reaction zones where they attack the reactants. Simplifying the chemical mechanism by removing the C_2-containing species produces significant differences in the predicted results only for the inner rich premixed reaction zone.   © 1999 by The Combustion Institute

INTRODUCTION

A triple flame is a partially premixed flame consisting of two premixed reaction zones (one fuel-rich and the other fuel-lean) and a nonpremixed reaction zone. The two premixed reaction zones form exterior "wings" of the flame. The nonpremixed reaction zone, that is established in the region where excess fuel and oxidizer from the respective rich and lean premixed reaction zones mix in stoichiometric proportion, is enclosed in between these two wings. All three reaction zones (that are often referred to as flames) merge at a "triple point." The loci of the "triple points" form a "triple line" in a planar configuration.

The behavior of triple flames is of fundamental importance for several reasons. First, triple flames may play an important role in the stabilization of laminar nonpremixed flames [1].

While premixed flames propagate because the flame provides heat to the unburned mixture, nonpremixed flames do not possess such a simple stabilization mechanism. The stabilization of nonpremixed flames can occur by two means: (1) near a splitter plate where the plate wake provides very low strain rates and where heat conduction to the plate becomes important; or (2) when the flames are lifted downstream in the form of a triple flame in which the propagating premixed reaction zones anchor the nonpremixed reaction zone [2]. Secondly, triple flames play an important role during reignition in turbulent flows when, after a local extinction due to excessive strain, the turbulence intensity decreases so that reignition can occur [3].

Triple flames were first reported by Phillips who investigated their propagation in a methane mixing layer in a horizontal configuration [4]. He was particularly interested in determining the flame speed and volume in the context of the explosive conditions that occur at the roof of

─────────

*Corresponding author. E-mail: ikpuri@uic.edu.

coal mine roadways. Thereafter, Dold performed a theoretical investigation that concluded that the triple flame propagation speed in the presence of a slowly varying mixture fraction gradient strongly depends upon the transverse mixture fraction gradient [5]. He determined that the flame speed increases as the mixture fraction gradient decreases, and it is bounded by the maximum adiabatic laminar flame speed of the system. The shape of triple flames was predicted to depend on the mixture fraction gradient, and theory found that flames bend at steeper gradients. In a subsequent study, Dold and Hartley relaxed the constraint of a slowly varying mixture fraction gradient and it was shown that the flame speed remains positive for all mixture fraction gradients that produce a reaction zone which is at least as thick as the preheat zone [6]. For very steep gradients negative flame speeds were predicted, which implied that triple flames could be established following the extinction of a diffusive interface [7].

Ruetsch et al. [1] theoretically investigated the effects of heat release and mixture fraction gradient on the flame speed. They concluded that heat release increases the flame speed, as does a decrease in the mixture fraction gradient, in accord with the results presented by Dold [5]. They found flame speeds to be higher than the corresponding planar premixed flame speed that was in disagreement with Dold, but in agreement with the experimental results of Phillips [4]. Ruetsch et al. suggested the following mechanism to explain their observations: The heat release causes the velocity component perpendicular to the flame to increase. As a consequence, the streamlines bend toward the centerline as they cross the flame. This results in a divergence of the velocity field ahead of the flame so that the velocity reaches a minimum at the triple point. They predicted that the minimum velocity, where the flame stabilizes, is close to the laminar flame speed (S_L), but the overall flame speed of the triple flame, which must be considered further upstream, is larger than S_L.

Kioni et al. [3] have reported on an experimental investigation of a lifted triple flame stabilized in a coflowing stream. They observed that the width of the premixed wings increases

as the mixture fraction gradient decreases. In addition, the velocity profile at the leading edge of a triple flame was examined as a function of the transverse mixture fraction gradient. A trend opposite to that predicted by Dold was observed [5], since the velocity increased with the mixture fraction gradient and was well above the adiabatic laminar flame speed of the corresponding stoichiometric premixed fuel–air mixture. However, Phillips [4] found the variation of the flame speed with the mixture fraction gradient to be consistent with the prediction by Dold [5]. Phillips suggested that the flame speed is higher for low mixture fraction gradients, because the flame is flatter and the preheating of the unburned mixture is more efficient under these conditions. However, the absolute flame speeds were higher than the adiabatic flame speed of the corresponding stoichiometric premixed flame. Kioni et al. [3] obtained a similar result by defining the flame speed as the mean flow velocity at the location of the flame.

Muniz and Mungal [8] experimentally investigated the velocity profile at the base of a lifted jet flame and found it to be similar to the prediction of Ruetsch et al. [1]. In particular, they observed that the flame stabilizes itself in the region where the velocity is close to the premixed laminar flame speed. Schefer and Goix [9] extended the work of Muniz and Mungal regarding the applicability of laminar triple flame concepts to the stabilization of lifted turbulent jet-flames, and concluded that this is not straightforward, since turbulence causes distortions in the velocity field. Muniz and Mungal found that the instantaneous velocity at the stabilization point varied between S_L to $3S_L$, while Schefer and Goix found that the average velocity at the instantaneous flame base increased from $0.2S_L$–$1.2S_L$ with increasing Reynolds number.

Aggarwal and Puri have reported on a numerical investigation of triple flame structure in axisymmeteric inverse lifted partially premixed flames [10]. They determined the existence of a spatially thin rich premixed flame (RPF), two spatially broad nonpremixed flames (NF) at either wing of the RPF, and a lean premixed flame (LPF) stabilized by heat and mass transport towards the oxidizer-rich center. Their investigation illustrated how triple flames can be

established in relatively complex configurations. Echekki and Chen [11] conducted direct numerical simulations of methanol–air triple flames and concluded that the triple region is strongly influenced by the reaction zone curvature and by the differential diffusion of molecular hydrogen. Both the curvature and diffusion effects augment radical production that, consequently, enhances the flame propagation speed. Echekki and Chen found that the flame structure could be characterized in terms of a mixture fraction parameter. A similar approach has been suggested by Aggarwal and Puri [10].

A divergence in the velocity field is caused by the combination of two factors: The heat release at the flame location, and the curvature of the flame front. However, both of these factors can be present in configurations other than those involving triple flames. Domingo and Vervisch [12] suggested that the front of the flame can propagate because of the interaction of multiple rich and lean layers (in accord with the conclusions of Aggarwal and Puri [10]). A fundamental understanding of this interaction is, therefore, required. Transport effects have also been investigated by Buckmaster and Matalon [13]. Despite the various questions, many aspects of triple flames have not been adequately investigated and are, consequently, not clearly understood.

In this study, laminar triple flames stabilized on a Wolfhard-Parker slot burner have been investigated by using detailed measurements and numerical simulations. As illustrated in Fig. 1, the flow consists of a rich mixture emerging from an inner slot and a lean mixture introduced from two symmetric outer slots. In this planar configuration the three reaction zones that characterize a triple flame are clearly distinguished. The measurements include those of the velocity field using laser Doppler velocimetry, the reaction zone location by detecting C_2^*-chemiluminescence, and the temperature distribution using laser interferometric holography. In addition, a detailed numerical model is employed to characterize the flame structure. It is based on C_2-chemistry and involves a mechanism containing 24 species and 81 reactions. A simplified and reduced form of this chemistry was employed by Plessing et al. [14] who determined that the triple flame structure depends on heat
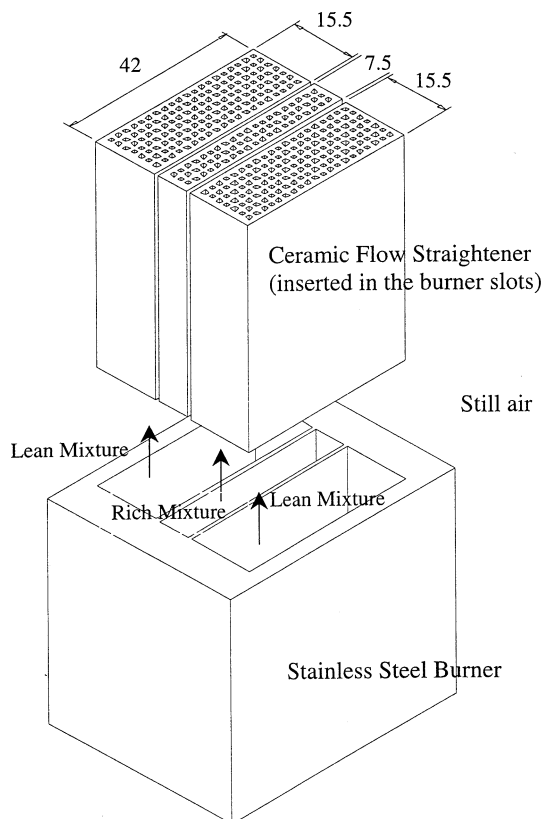

Fig. 1. A schematic diagram of the Wolfhard-Parker slot burner. The burner dimensions are in units of mm.

transport between the multiple reaction zones, and on the heat loss from the curved reaction zone fronts in the vicinity of the triple point.

The numerical and chemical models are validated through comparisons with experimental measurements for a representative flame. The discussion focuses on the detailed structure of this triple flame, the interactions between the three reaction zones, and the dependence of the flame structure on the initial velocity and mixture ratio.

EXPERIMENTAL PROCEDURE

Atmospheric methane–air flames were established using a Wolfhard-Parker slot burner. A schematic diagram of the burner is contained in Fig. 1. The flows were straightened and laminarized in the inner and outer burner slots using ceramic inserts. The rectangular burner geometry provided symmetrical two-dimensional flames.
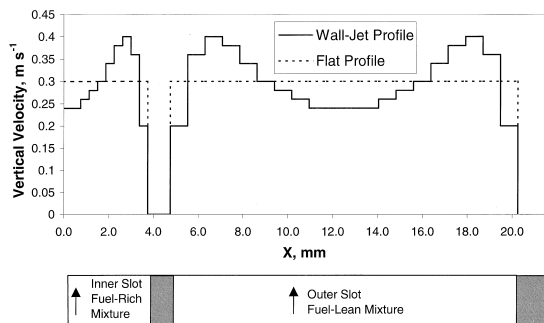
Fig. 2. The velocity profile at the inlet boundary. The wall jet and bulk-averaged profiles correspond to the same volumetric flow rate.

Velocity Measurements

A laser Doppler velocimeter (DANTEC 5500A with an Ar-ion laser) was used to make the velocity measurements. The flow was seeded with TiO_2 particles. A traverse controller was used to make the point measurements in a specified domain. Despite the insertion of ceramic flow straighteners in the burner slots (cf. Fig. 1), cold flow measurements showed the formation of wall jets in each of the three slots. The flow retained its two-dimensional characteristics, but a higher gas velocity was measured adjacent to the walls than at planes removed from it. A typical velocity profile and the associated bulk-averaged velocity is presented in Fig. 2. This profile was used as a boundary condition for the simulations. Although the measured rms velocities were, in general, small, their values were used as a criterion to evaluate the measurement accuracy for axial velocities greater than 0.2 m s^{-1}. When the local mean axial velocity was greater than 0.2 m s^{-1}, velocity measurements with rms values greater than 5% of the mean were assumed to be contaminated with noise, and, therefore, discarded.

C_2^* Chemiluminescent Emission

The excited C_2^* free radical species is considered to be a good indicator of the reaction zone [15], and its light intensity varies linearly with the volumetric heat release [16, 17]. The C_2^*-chemiluminescence images were obtained from flames using a 513×480 pixel intensified and gated solid state camera (ITT F4577). A narrow wavelength interference filter (470 ± 10 nm) was employed to detect the emission occurring at 473 nm due to the (1, 0) C_2 Swan band [18]. A background image was subtracted from the raw images to correct for noise. The chemiluminescence images are directly proportional to the C_2^* formation rate and, therefore, serve as a qualitative rate measure of the flame chemistry [19].

Temperature Measurements

A nonintrusive diagnostic tool is required to measure the temperature in triple flames, since the spatially broadened reaction zones produce unquantifiable errors due to conduction effects when thermocouples are used. We have determined that laser holographic interferometry is a suitable tool to measure the temperature of two-dimensional partially premixed flames [20]. The use of holographic interferometry to obtain refractive index and temperature measurements in flames has been described in detail in the literature [21–23].

A double-exposure laser image holographic technique is used for measuring the temperature field. A typical off-axis holography system is used. The beam from a 17 mW He-Ne laser is divided by a beam splitter into an object and a reference beam. The object beam passes through the flame in a direction parallel to the horizontal (z-) axis. The wave front experiences a two-dimensional refractive index distribution in the other two directions. A holographic plate sensitive to red light is used to record the refractive index distribution. The temperature can be related to the refractive index through the relation $T = (n_0 - 1) T_0/(n_0 - (N\lambda)/L - 1)$, where N denotes the fringe number (inferred from the hologram image), n_0 represents the reference refractive index at the reference temperature T_0, λ the wavelength, and L the beam path-integration length (related to the burner dimension in the cross-stream direction).

NUMERICAL MODEL

The numerical model solves the time-dependent governing equations for a two-dimensional

reacting flow. Using Cartesian coordinates (x, y), these equations can be written in the form

$$\frac{\partial(\rho\phi)}{\partial\dagger} + \frac{\partial(\rho u\phi)}{\partial x} + \frac{\partial(\rho v\phi)}{\partial y} = \frac{\partial}{\partial x}\left(\Gamma^\phi \frac{\partial\phi}{\partial x}\right)$$

$$+ \frac{\partial}{\partial y}\left(\Gamma^\phi \frac{\partial\phi}{\partial y}\right) + S^\phi, \quad (1)$$

where ρ denotes density, and u and v the transverse (x) and axial (y) velocity components, respectively. The general form of the equation represents the mass, momentum, species, and energy conservation equations, depending on the variable represented by ϕ. The transport coefficient Γ^ϕ and the source terms S^ϕ appearing in the governing equations are provided in Table 1 of Ref. 24. The set of governing equations is completed by introducing the overall species conservation equation and the state equation $p = \rho R_u T\Sigma_i Y_i/M_i$ (where R_u denotes the universal gas constant, T the temperature, and M_i the molecular weight of the ith species). The thermodynamic and transport properties appearing in the above equations are considered to be temperature- and species-dependent. First, the viscosity and thermal conductivity of the individual species are estimated based on Chapman-Enskog collision theory, following which the mixture properties are determined using the Wilke semi-empirical formulae. Chapman-Enskog theory and the Lennard-Jones potentials are employed to calculate the binary-diffusion coefficient D_{i-N_2} between each species and nitrogen. The enthalpy h and specific heat are calculated for each species using the polynomial curve fits from Ref. 25.

Two chemical mechanisms are employed. The first is based on a global one-step, 5-species chemistry that provides a steady-state solution. It is used to simulate the ignition of the mixture (by an artificial decrease in the activation energy) and to provide a first estimate that is used as input data for the second mechanism. This mechanism is based on a detailed multistep model with 24 species and 81 reactions [26]. The effect of the input data from the global mechanism becomes negligible after a few hundred iteration cycles.

The computational domain is bounded by the symmetry plane and an outflow boundary in the transverse direction and by the inflow and another outflow boundary in the axial direction. Symmetric conditions are applied at the left boundary, whereas those at right boundary correspond to a free surface. At the inflow boundary, except for the wall where no-slip boundary conditions are imposed, uniform velocity profiles are assumed for both the inner fuel-rich and outer fuel-lean streams. The temperature and species mass fraction profiles are also assumed to be uniform at the inflow boundary. The flow variables at the outflow boundary are obtained using an extrapolation procedure with weighted zero and first-order terms. The main criterion used in selecting the weighting functions is that the flow should exit the outflow boundary without being distorted. In addition, the outflow boundaries in both directions are located sufficiently far from the respective inflow and symmetric boundaries so that the propagation of boundary-induced disturbances is minimized. The boundary conditions are chosen to match the general experimental settings with the species' densities and the mixture velocity at the inflow boundary. Moreover, the dimensions of the domain are large enough to minimize the effect of the propagation of disturbances into the region of interest.

The computational model is based on the algorithm developed by Katta et al. [27]. An implicit algorithm is employed to solve the unsteady gas-phase equations. The governing equations are integrated by using a "finite control volume" approach with a staggered, nonuniform grid system (131×88). Grid lines are clustered near the flame surfaces to resolve the steep gradients of the dependent variables. An iterative Alternating Direction Implicit (ADI) technique is used for solving the resulting ($N_s + 3$) sets of algebraic equations. A stable numerical-integration procedure is achieved by coupling the species and energy equations through the chemical-reaction source terms. At every time step, the pressure field is calculated by solving the pressure Poisson equations at all grid points simultaneously and utilizing the LU (Lower and Upper diagonal) matrix-decomposition technique. Further details about the numerical model and the computational algorithm can be found in Refs. 26, 27, and 28.

RESULTS AND DISCUSSION

General Features of Triple Flames

The triple flames that are investigated consist of three distinct reaction zones. The inner region contains a bow-shaped rich premixed reaction zone. Likewise, there are two symmetric lean premixed reaction zones in the outer region. A nonpremixed reaction zone is contained between the two (lean and rich) premixed reaction zones. This structure is evident from the C_2^*-chemiluminescence image obtained from a representative flame that is presented in Fig. 3. For all the cases investigated, the inner reaction zone was found to be spatially and temporally stable. On the other hand, the nonpremixed reaction zone and, in particular, the outer premixed zone tended to flicker. Only in a few cases it was possible to establish an overall stable triple flame.

Figures 4 and 5 contain images of the C_2^*-chemiluminescence intensity for various cases and present the influences of velocity and equivalence ratio variations on the triple flame structure. For the images presented in Fig. 4, the overall equivalence ratio $\phi_{overall}$, and the inner and outer velocities (respectively, denoted by v_{in} and v_{out}) were kept constant ($\phi_{overall} = 0.6$, $v_{in} = v_{out} = 0.3$ m s^{-1}), while the inner and the outer equivalence ratios, respectively denoted by ϕ_{in} and ϕ_{out} were progressively varied in the range $1.6 \leq \phi_{in} \leq 1.9$, and $0.33 \leq \phi_{out} \leq 0.39$. For flame (a) in Fig. 4: (1) the inner reaction zone height is relatively small, (2) the nonpremixed reaction zone is luminous until its apex, and (3) the lean premixed reaction zone is faintly luminous. As ϕ_{in} increases (or, conversely, as ϕ_{out} decreases), the gradient $\nabla\phi$ becomes larger, and we find that (1) the inner rich premixed and the nonpremixed reaction zones grow in height, (2) the nonpremixed zone loses luminous intensity near its tip, (3) the lean premixed region becomes even less luminous and moves spatially closer to the nonpremixed region until the two are almost undistinguishable (as illustrated by flame (d) in Fig. 4).

For the flames presented in Fig. 5 the global equivalence ratios are held constant ($\phi_{overall} = 0.6$, $\phi_{in} = 1.8$, $\phi_{out} = 0.35$), while the inner and the outer velocities are varied from 0.2 to 0.4 m

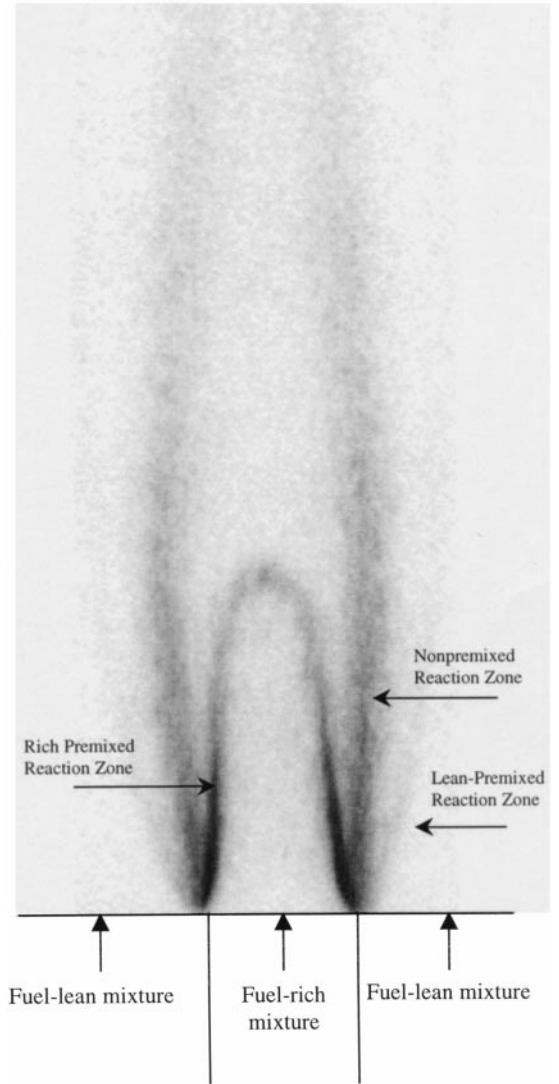Fig. 3. C_2^*-chemiluminescence image of a triple flame established at $\phi_{overall} = 0.6$, $\phi_{in} = 1.8$, $\phi_{out} = 0.35$, and bulk-averaged velocities $\bar{v}_{in} = 0.3$ m s^{-1}, $\bar{v}_{out} = 0.3$ m s^{-1}.

s^{-1}. The effect of the velocity increase is similar to that of varying the inner equivalence ratio, although at higher velocities the nonpremixed reaction zone tips are weaker, and the lean premixed reaction zone becomes less visible. For flame (d) in Fig. 4 and flame (c) in Fig. 5, the outer lean premixed and the nonpremixed reaction zones tend to flicker. The flickering intensity becomes stronger as the inner equivalence ratio is increased.

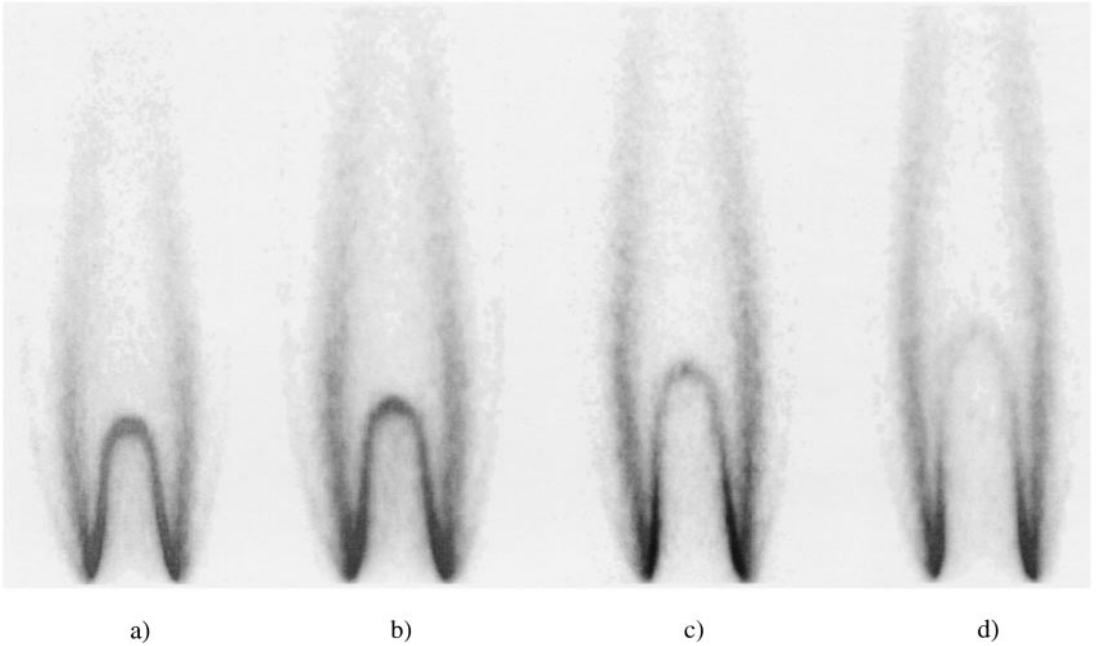Figures 4 and 5 demonstrate that increases in the equivalence ratio (above stoichiometric) or

Fig. 4. Effect of varying equivalence ratio on the global flame structure ($\phi_{overall}$ = 0.6, and bulk-averaged velocities $\bar{v}_{in}$ = 0.3 m s^{-1}, $\bar{v}_{out}$ = 0.3 m s^{-1}). (a) ϕ_{in} = 1.6, ϕ_{out} = 0.39; (b) ϕ_{in} = 1.7, ϕ_{Out} = 0.37; (c) ϕ_{In} = 1.8, ϕ_{Out} = 0.35; (d) ϕ_{In} = 1.9, ϕ_{Out} = 0.33.

in the coflow velocity produce similar effects on the flame shape. The trend in both figures is very similar, progressing from left to the right. The reaction zone topography establishes itself along locations where the flow residence time approaches the time required for the chemical reactions to proceed with significant rates. The

Fig. 5. Effect of varying the inflow velocity on the global flame structure represented by the C$_2^*$-chemiluminescence ($\phi_{overall}$ = 0.6, ϕ_{in} = 1.8, ϕ_{out} = 0.35). (a) Bulk-averaged velocities $\bar{v}_{in} = \bar{v}_{out}$ = 0.2 m s^{-1}; (b) $\bar{v}_{in} = \bar{v}_{out}$ = 0.3 m s^{-1}; (c) $\bar{v}_{in} = \bar{v}_{out}$ = 0.4 m s^{-1}.

flow residence time decreases as the velocity is raised and, consequently, the flame stabilizes further downstream. When the equivalence ratio is lowered, the chemical time decreases and the flame stabilizes further downstream in this case as well.

Uncertainty Analysis

We now provide an estimate for the uncertainties in the inflow boundary conditions. The uncertainties in the inflow velocity and equivalence ratio depend on uncertainties in the volumetric flow rates Q of fuel and air that are controlled by flowmeters and pressure gages. The flow uncertainty w_Q depends upon the uncertainties in the flowmeter and pressure gage settings (respectively denoted by w_r and w_p) through the relation $w_Q = [(w_r \partial Q / \partial r_f)^2 + (w_p \partial Q / \partial p)^2]^{1/2}$ [29], where r_f and p, respectively, denote the flowmeter reading and the pressure setting. The analysis for this case resulted in uncertainties of 3.75% and 0.95%, respectively, for the inner and outer air flows, and of 5.7% and 5.5%, respectively, in case of
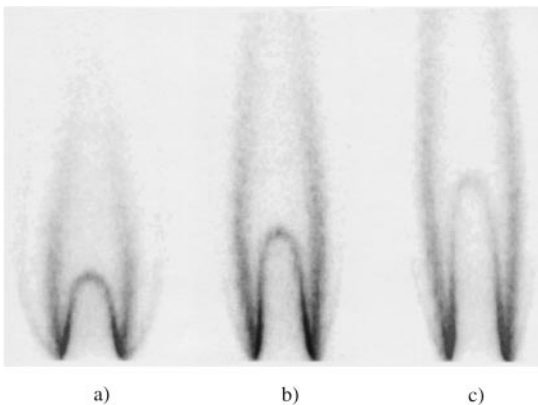
the inner and outer fuel flows. This produced uncertainties of 3.3% and 1%, respectively, in the inner and outer velocities, and of 7.4% and 6.4%, respectively, for the inner and outer equivalence ratios.

Comparison between Numerical and Experimental Results

A representative flame is now discussed corresponding to the conditions $\phi_{overall} = 0.6$, $\phi_{in} = 1.8$, $\phi_{out} = 0.35$, and bulk-averaged velocities $\bar{v}_{in} = \bar{v}_{out} = 0.3$ m s^{-1}. We have previously mentioned that a uniform bulk-averaged velocity cannot be assumed at the inflow boundary, since the measured velocity profile is nonuniform due to the formation of wall jets. The simulations were found to be sensitive to the inflow velocity profile. In particular, the inner rich premixed flame (based on the reaction zone thickness) was located in the range 16.5–18 mm when the nonuniform velocity profile shown in Fig. 2 was employed, and from 15–16.5 mm when a uniform inflow velocity was assumed. The former values are closer to the experimentally measured inner flame height that lies in the range 18–20 mm (based on the C_2^*-chemiluminescence images). Therefore, subsequent discussion of the simulations is based on the nonuniform inflow velocity profile.

The inner premixed and central nonpremixed reaction zones flicker with a negligible amplitude, the maximum intensity of which is ~0.2 mm. The outer lean premixed reaction zone flickers with a maximum amplitude of ~1 mm. However, in all cases the flicker amplitude is negligible at locations nearer the burner, and assumes larger values further downstream. The flickering frequency is ~12 Hz. The CCD camera samples at a rate of 16 Hz. Therefore, the experimentally obtained images exhibit some averaging effects and the lean premixed reaction zone appears thickened at downstream locations.

The computed volumetric heat release rates are compared with the experimentally measured C_2^*-chemiluminescence intensities [16]. A similar validation of the numerical model has been previously reported for partially premixed flames containing two reaction zones [17, 28]. The C_2^* chemiluminescence image and the predicted heat release rates are compared in Fig. 6.

The predicted flame shape is found to be in excellent agreement with the spatial profile of the measured chemiluminescence intensity. While the locations of the rich premixed and the nonpremixed reaction zones are in agreement, the lean premixed reaction zone appears to have a weaker chemiluminescent intensity than the predictions indicate. This is due to the different chemistry present in the various zones. The reactions, such as $CH_4 + H \rightarrow CH_3 + H_2$, that generate CH_3 and, consequently, C_2^* radicals are relatively weaker in the outer lean premixed reaction zone. The heat release in that zone is primarily due to HO_2 chemistry, which eventually leads to water formation. The specific heat release rate contours of the reactions $O_2 + H + M \Leftrightarrow HO_2 + M$ and $HO_2 + OH \rightarrow H_2O + O_2$ are presented in Fig. 7. The heat release due to these reactions is of the same order as that of the total heat release in the outer reaction zone. However, the C_2^*-chemiluminescence measurements do not accurately reproduce this component of the heat release, since C_2^* radicals are formed due to a different chemical pathway.

The height of the inner reaction zone (which is in the range 18–20 mm) is well predicted. In addition, the measured and predicted shapes and widths of the two outer (nonpremixed and lean premixed) reaction zones are in good agreement. It is impossible to avoid edge effects that occur at the front and back edges of the burner. There, the flame is not fully two-dimensional, since it is distorted by its environment. Consequently, the measured image exhibits some noise.

Figure 8 presents a comparison between the holographic measurement and the numerical prediction. The measurement is represented by the raw image of the refractive index distribution, where each fringe corresponds to a different temperature value. (In the present study only a qualitative comparison is provided. Due to edge effects and flow divergence, the beam path-integration length varies in the axial direction, so that an accurate inference of L is nontrivial. A more quantitative comparison will be presented in Ref. 20.)

There is excellent qualitative agreement between the measurement and the prediction, and both show that the inner reaction zone height
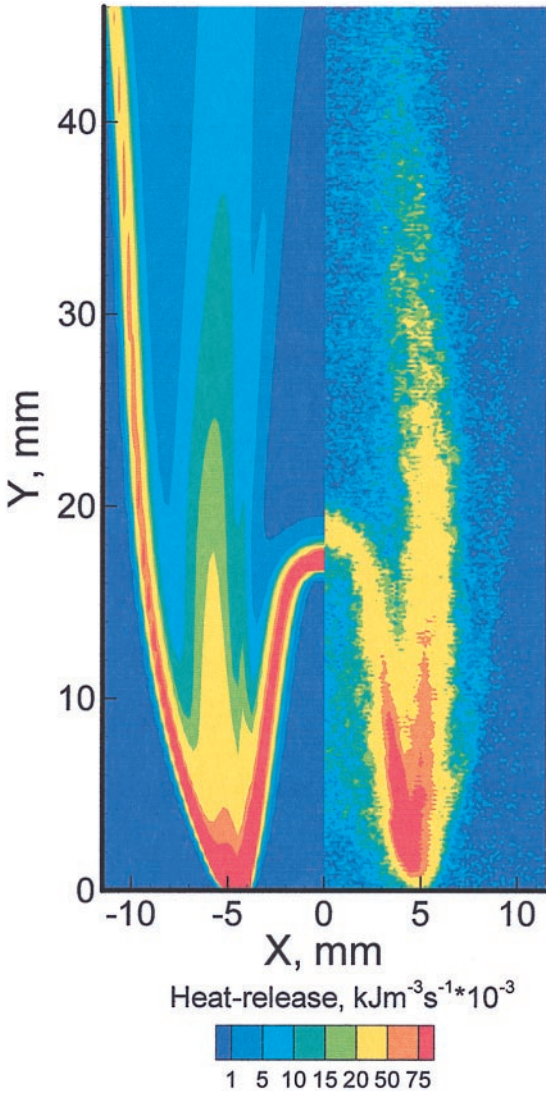
Fig. 6. Comparison between the predicted heat-release contours (left) and an experimentally obtained C_2^*-chemiluminescence image (right) for the flame described in Fig. 3. The chemiluminescence image has been modified by multiplying each pixel intensity by a constant value defined by the ratio of the maximum specific heat release to the maximum pixel intensity.
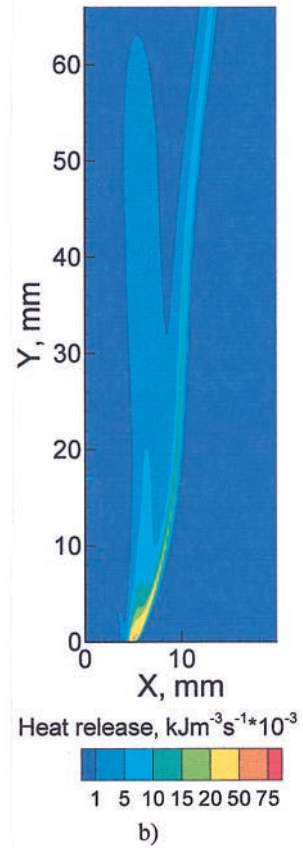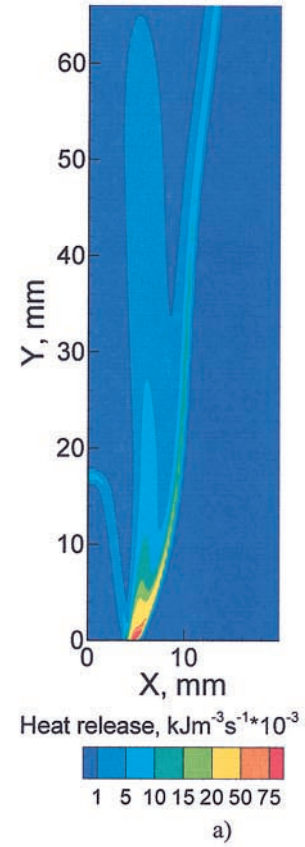
Fig. 7. Specific heat release rate contours due to the following reactions:
(a) $O_2 + H + M \Leftrightarrow HO_2 + M$
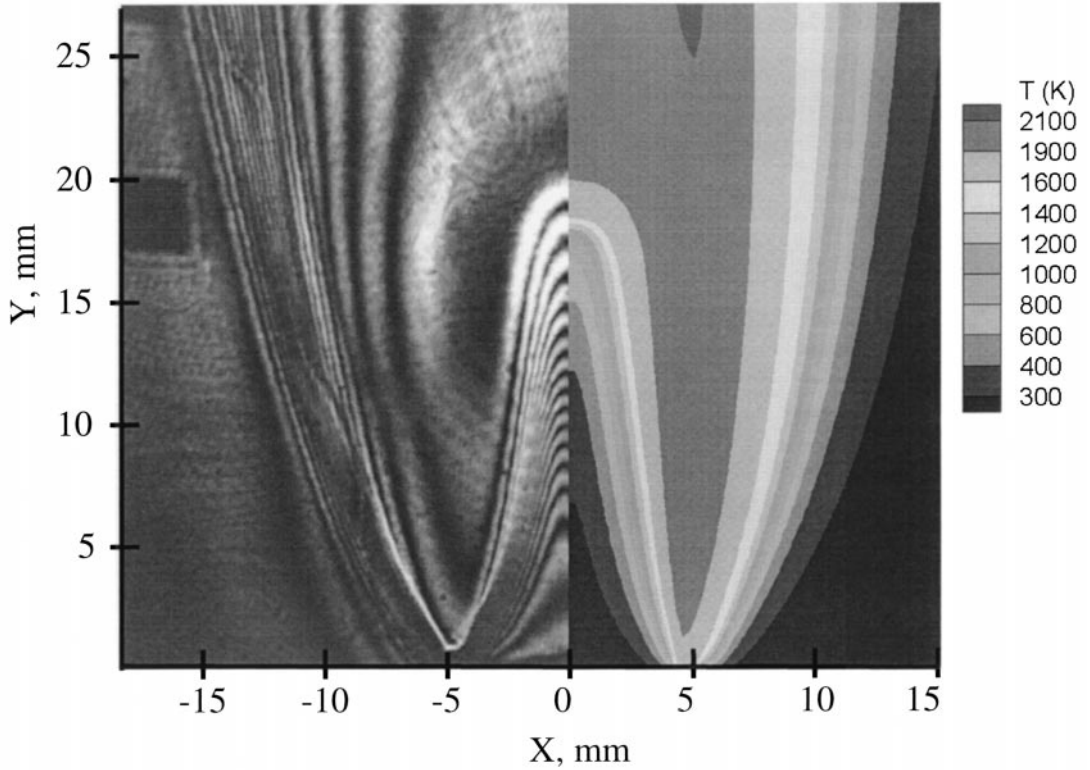(b) $HO_2 + OH \rightarrow H_2O + O_2$.

Fig. 8. Comparison between the holography measurements (left) and the numerical prediction (right) of the temperature distribution for the flame described in Fig. 3. The holography measurement is represented by an image of the refractive index distribution.

lies in the range 18 to 19 mm. This will be corroborated by a comparison between the measured and predicted velocity fields. The inner rich premixed reaction zone is anchored to the slot burner walls, where both the preheat and reaction zone thicknesses are relatively small. Moving away from the walls towards the centerline, the temperature gradients decrease, and both of these zones are spatially broad. Both the measurements and the prediction are in agreement regarding this variation in the thickness of the two zones. It is not possible to distinguish the outer lean premixed flame from the temperature distribution alone. This is due to the synergistic heat transfer from the nonpremixed reaction zone to the outer lean premixed region. The highest temperatures occur in the spatial region between the inner rich premixed and the nonpremixed reaction zones. Although the general shape of the flame is well-predicted, the holographic measurements indicate a slightly steeper temperature gradient across the

inner reaction zone. This small discrepancy probably arises due to non-negligible heat transfer to the burner during the experiments.

Figures 9 and 10 present a comparison between the measured and the predicted velocities. The predicted heat release rates are also illustrated in Fig. 9 so that the location of the three reaction zones can be easily identified. There is excellent qualitative agreement between the measured and predicted velocities. Figure 9 shows that the outer flow is entrained towards the centerline due to buoyancy effects, in accord with previous predictions regarding gravitational effects on partially premixed flames [28]. The heat release produces dilatation effects normal to the inner and outer premixed reaction zones. Buoyancy effects entrain the oxidizer from the lean outer flow and transport it to the nonpremixed reaction zone, so that the velocity vectors turn towards the centerline. Note that the flow appears to accelerate along the nonpremixed reaction zone.
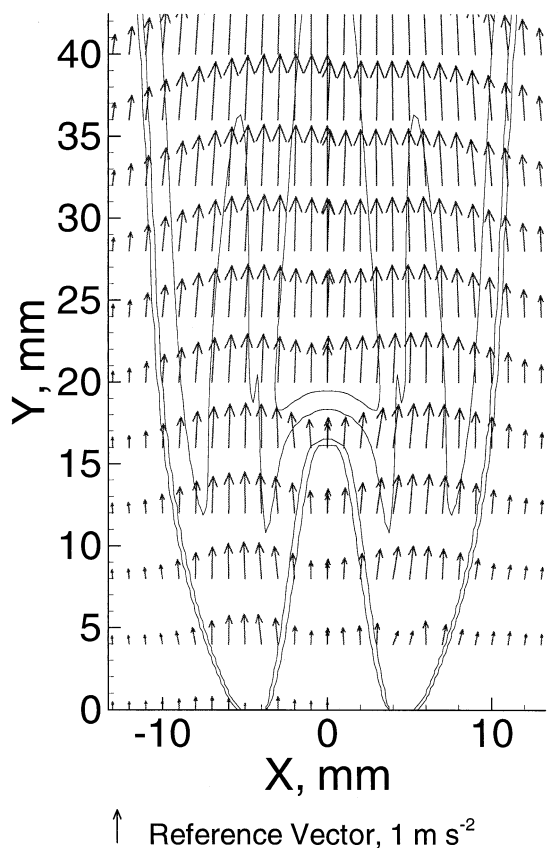
Fig. 9. Comparison between the measured (left) and predicted (right) velocity profiles of the flame described in Fig. 3. The predicted heat release rate contours are superimposed in order to identify the location of the various reaction zones.

A more quantitative comparison is presented in Fig. 10 which shows the measured and predicted axial velocity profiles at four different transverse locations. There is excellent agreement between the measured and predicted velocities, within experimental uncertainty, although in the middle of both the inner ($x = 0$ mm) and outer ($x = 10$ mm) slots the measured velocity appears to be slightly larger than the predictions. Along the centerline at $x = 0$ mm the expansion due to the heat release from the inner reaction zone occurs between 17–18 mm and, taking the experimental uncertainties into account, the measurements and predictions are in good agreement.

Chemical Pathways

In order to investigate interactions between the reaction zones and to identify the dominant chemical pathways, the reaction rates have been integrated (1) over the entire domain, and (2) over spatial regions that are selected to illustrate both the dominant chemical pathway in a reaction zone of interest and the interactions between the various zones (as illustrated in Fig. 11). The overall impact of a particular reaction on the system can be inferred by integrating its rate over the entire domain. Consequently, the dominant chemical pathways can be determined.

As illustrated in Fig. 12, the methane consumption pathway consists of (1) a gradual substitution of H-atoms with O-atoms (oxidation) by O_2 and OH that is produced through the $O_2 \rightarrow H_2O$ path (2) and hydrogen abstraction by H-atoms. The path leading to H_2O is more complex and consists of a reduction of the molecular oxygen in the initial mixture due to H-atom attack. In addition, radicals produced through the $CH_4 \rightarrow CO_2$ path, such as CH_2O and CHO, can react with O_2 and OH radicals and are also responsible for the reduction.

A more detailed investigation shows that the relative importance of each pathway varies in the different reaction zones, i.e., rich premixed, lean premixed, and nonpremixed. Figure 13 presents the values of the integrated rates of the major reactions in different regions, and it will serve as a reference for the following sections in which the features of each zone are discussed.

Inner Rich Premixed Reaction Zone

The pathways involved with methane conversion to CO_2 are illustrated in Fig. 12a. Path 1 accounts for 67% of CH_3 consumption, Path 2 for 18%, and Path 3 for 15%. The relative importance of Paths 2 and 3 is higher in the rich premixed zone compared to the other two reaction zones. Molecular hydrogen, which is an important intermediate species, is produced during each step involved with Path 2. Path 3 involves all of the C_2-radicals. Many radical species are produced through this path, which accelerates the overall process. As shown in the figure, excess methane leaks through the rich premixed reaction zone and is consumed in the nonpremixed reaction zone.

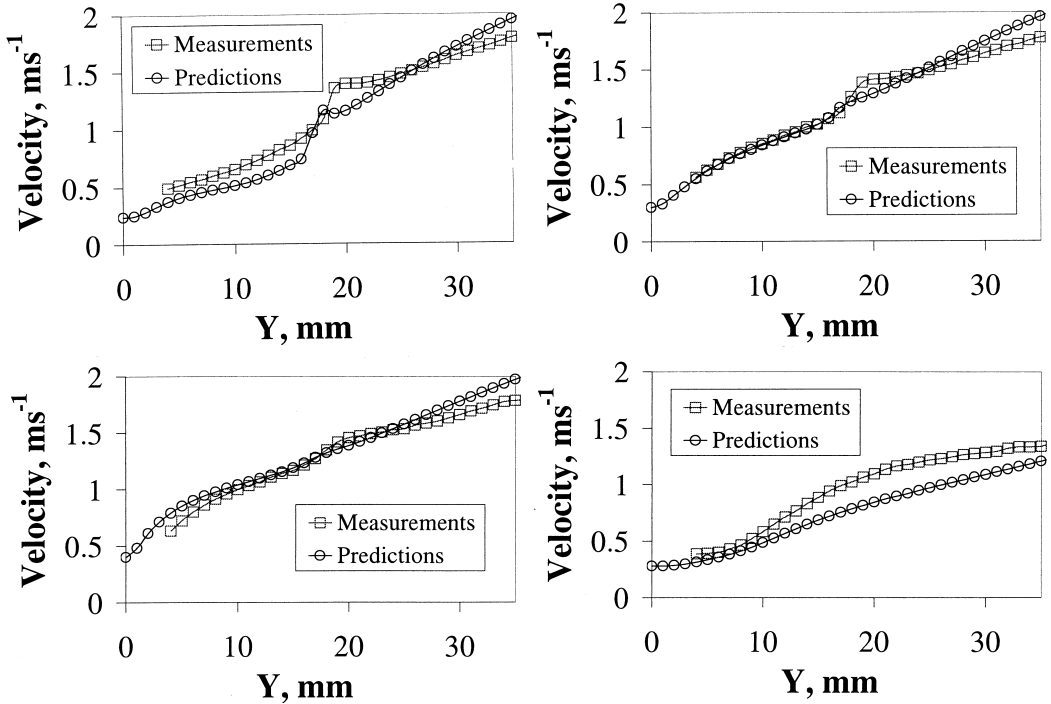Molecular oxygen reacts according to the reactions

Fig. 10. Comparison between measured and predicted axial velocity profiles at four different transverse locations: (a) $x = 0$ mm (centerline), (b) $x = 2$ mm (above the plane of the inner slot), (c) $x = 3$ mm (above the inner slot edge), (d) $x = 10$ mm (above the plane of the outer slot).

$$O_2 + H \Leftrightarrow OH + O, \text{ and} \qquad (I)$$

$$O_2 + H + M \Leftrightarrow HO_2 + M. \qquad (II)$$

Reaction I produces hydroxyl radicals, while HO_2, which is produced in Reaction II, reacts either with H to give OH (70% of the HO_2 consumption rate) or with OH and H to give H_2O (30% of HO_2 consumption).

The concentration of H_2 and CO, which are important intermediate species produced in the inner rich premixed reaction zone, reaches a maximum value at the tip of this zone (10 mm). Thereafter, they diffuse toward the nonpremixed reaction zone where CO is oxidized to CO_2 and H_2 reacts with OH (that is mainly produced through Reaction V, and is discussed below) through the reaction

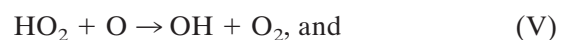$$H_2 + OH \Leftrightarrow H_2O + H. \qquad (III)$$

This reaction produces water and H-atoms, which sustain combustion by attacking CH_4, CH_3, and CH_2.

Outer Lean Premixed Reaction Zone

In the outer lean premixed region, methane and molecular oxygen are mixed in less than stoichiometric proportion. Therefore, excess O_2 leaks through this reaction zone to the nonpremixed reaction zone. The dominant reactions by which O_2 is depleted are identical to those in the rich premixed flame (Reactions I and II). However, the rates of these reactions are higher (two times as strong) in the lean premixed region zone than in the rich premixed reaction zone. Overall, reactions are likely to be stronger in the rich premixed reaction zone than in the lean region due to the higher temperature there, but in this case the higher O_2 concentration more than compensates for the lower temperatures.

The HO_2 formed due to Reaction II reacts as follows:

$$HO_2 + OH \rightarrow H_2O + O_2, \qquad (IV)$$

$$HO_2 + O \rightarrow OH + O_2, \text{ and} \qquad (V)$$
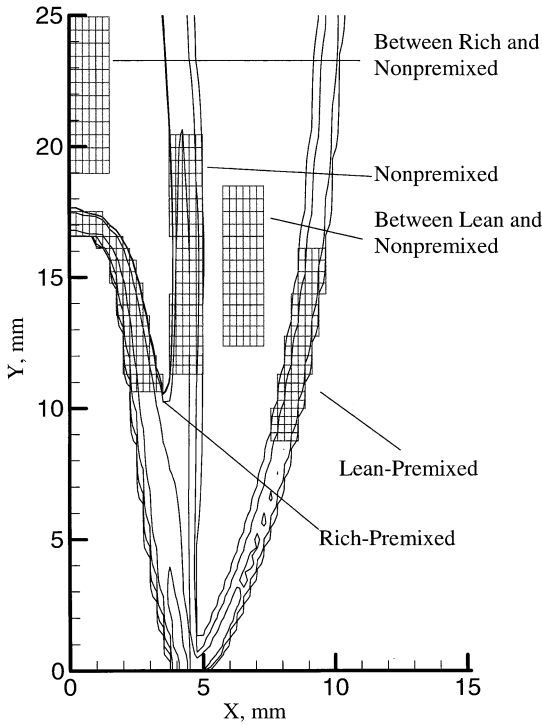
$$HO_2 + H \rightarrow OH + OH. \qquad (VI)$$

Fig. 11. Selected reaction zones in the triple flame where specific reaction rates have been integrated to investigate the differences between the reaction zones.

Reaction IV (which accounts for 60% of the HO_2 consumption rate) and Reaction V (8% of HO_2 consumption) lead to the formation of H_2O and O_2, whereas Reaction VI (25%) forms OH radicals. This is different from the pathways that occur in the inner premixed zone, where 70% of the HO_2 consumption is due to Reaction VI through which OH radicals are formed. Therefore, whereas the HO_2 chemistry in the rich premixed zone consists of propagation reactions, in the lean premixed region it consists primarily of termination reactions. Water is formed mainly through the HO_2 chemistry in the lean region rather than through Reaction V, due to the relatively low concentrations of H_2.

Methane consumption occurs along Path 1 of Fig. 12a, since 97% of CH_3 consumption rate is due to reactions that lead to CH_2O. Path 2 is much weaker here than in the rich premixed reaction zone due to the relatively lower H-atom concentrations. Path 3 (involving C_2-species) is much weaker in the lean premixed zone due to the relative scarcity of C-atoms. Unlike
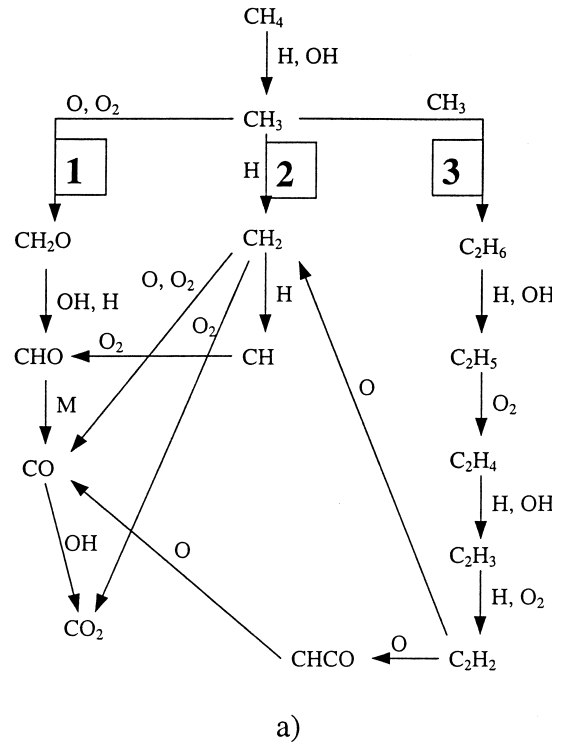
a)
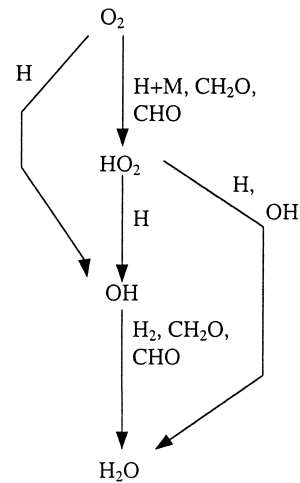
b)

Fig. 12. Identified reaction pathways for (a) $CH_4 \rightarrow CO_2$ conversion, and (b) $O_2 \rightarrow H_2O$ conversion.

in the rich premixed zone, CO does not diffuse toward the nonpremixed zone, but is immediately oxidized to form CO_2. The $CH_4 \rightarrow CO_2$ pathway proceeds due to reactions involving species such as O, O_2, and OH rather than
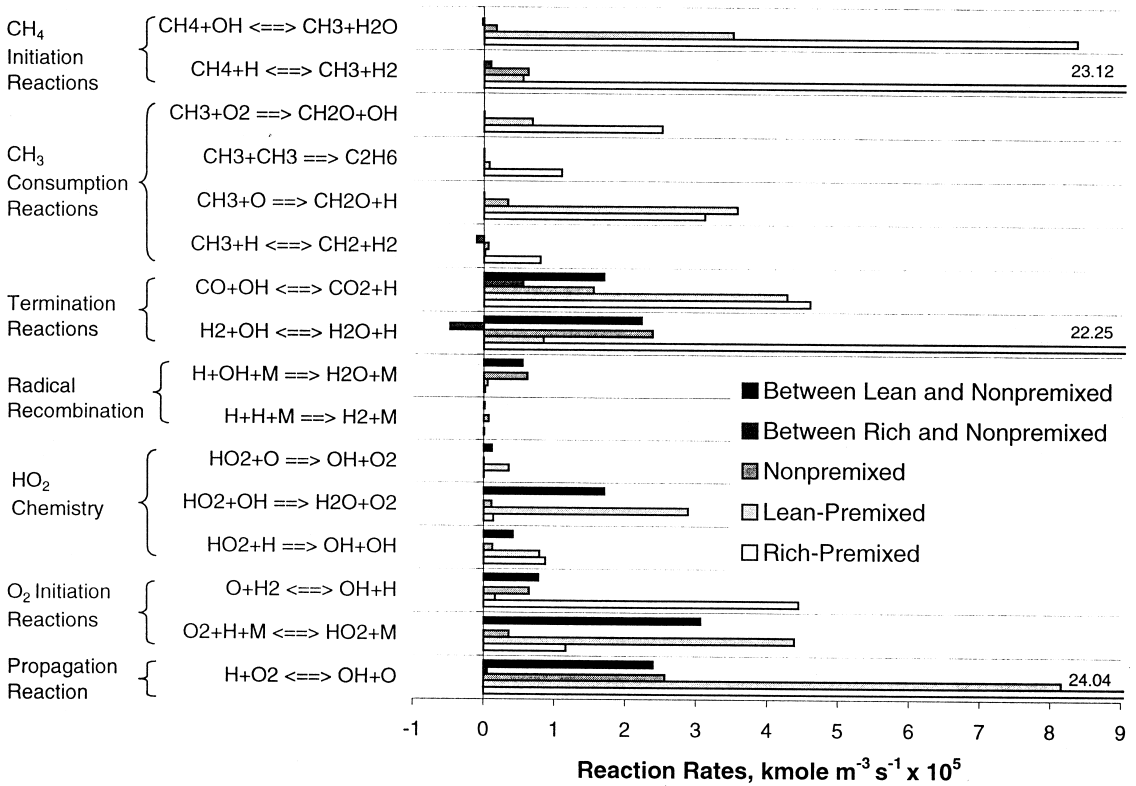
Fig. 13. Comparison among the average rates of the significant reactions in the various reaction zones.

H-atoms. For instance, during the $CH_2O \rightarrow CHO$ conversion step, the radicals responsible for the reaction, listed in order of importance, are H, OH, and O in the rich premixed reaction zone, and OH, O, and H in the lean premixed region.
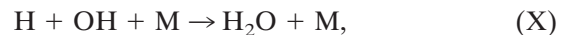
Nonpremixed Reaction Zone

The nonpremixed reaction zone lies in between the rich and lean premixed flame zones where methane, the intermediate species CO and H_2, and O_2 meet in stoichiometric proportions. The local temperatures are relatively higher here and, accordingly, the concentration of radicals is also large. Methane consumption follows Path 1 of Fig. 12a, since 96% of CH_3 consumption rate occurs due to reactions that lead to CH_2O formation.

Molecular hydrogen reacts through reactions VII and VIII, namely,

$$O + H_2 \Leftrightarrow OH + H, \text{ and} \qquad (VII)$$

$$H_2 + OH \Leftrightarrow H_2O + H. \qquad (VIII)$$

The consumption of molecular hydrogen leads to the formation of water and other radical species. The radical concentration is high in this zone, and the following termination reactions involving H-atoms

$$H + H + M \rightarrow H_2 + M, \text{ and} \qquad (IX)$$

$$H + OH + M \rightarrow H_2O + M, \qquad (X)$$

are particularly important.

In summary, radical activity is higher in the nonpremixed reaction zone than in the other reaction zones. Overall, radicals from the nonpremixed reaction zone are transported to both the rich and lean premixed reaction zones where they attack the reactants. The interactions among the three reaction zones are schematically illustrated in Fig. 14.

Region between the Rich Premixed and Nonpremixed Reaction Zones

This region is characterized by low reaction rates compared to those that occur in the two
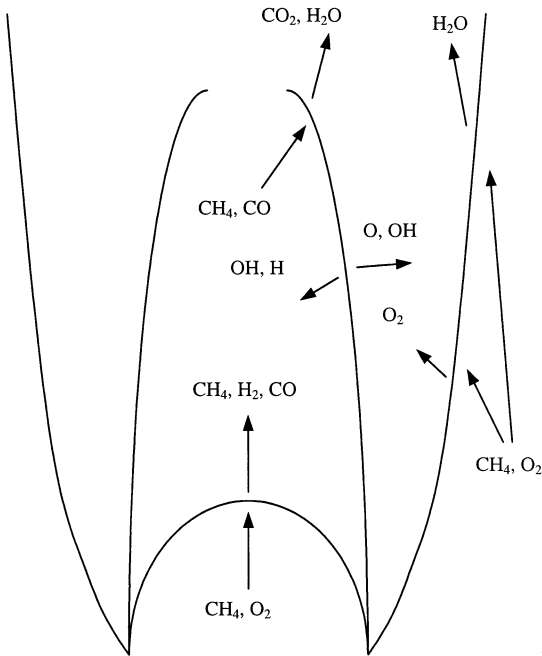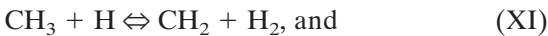
Fig. 14. Schematic illustration of the interactions between the various reaction zones.

adjacent reaction zones. However, there are some important features worth noting. Reactions VII and VIII proceed in the reverse direction as do the reactions

$$CH_3 + H \Leftrightarrow CH_2 + H_2, \text{ and} \qquad (XI)$$

$$CH_4 + OH \Leftrightarrow CH_3 + H_2O. \qquad (XII)$$

Therefore, the reactants of the rich premixed zone are slightly reformed in this region due to the relatively high temperatures and product concentrations.

Region between Lean Premixed and Nonpremixed Reaction Zones

In this region reactions along the $O_2 \rightarrow H_2O$ path have relatively large rates, while the $CH_4 \rightarrow CO_2$ path is weaker compared to other portions of the flame. As illustrated in Fig. 13, the magnitude of reactions such as $O_2 + H + M \Leftrightarrow HO_2 + M$, $HO_2 + H \rightarrow OH + OH$, and $H_2 + OH \Leftrightarrow H_2O + H$ is the same as in the rich and lean premixed flame zones.

Another important feature of this region is that the radical concentrations are relatively high. Consequently, reactions involving radical

recombination, such as $H + OH + M \rightarrow H_2O + M$ exhibit the largest reaction rates here.

Influence of C_2-chemistry

We have investigated the impact of simplifying the chemistry by removing the C_2-containing species from the simulation. Recall that Path 1 (which involves only C_1-containing species) accounts for over 95% of the CH_3 consumption rate in the lean premixed and nonpremixed reaction zones, even when the C_2-mechanism is employed. Therefore, upon simplification of the mechanism, significant differences occur only in the inner rich premixed reaction zone. This zone is predicted to extend from 14–16 mm along the centerline by the C_1-mechanism, while the corresponding simulation due to the C_2-mechanism provides the range extending from 16–18 mm. The higher inner rich premixed reaction zone height is a consequence of the relatively slower chemistry that occurs along Path 3 in rich mixtures, since some critical rates are dependent on the local O_2 concentration.

Role of Heat Loss

Heat loss to the burner can play a significant role in anchoring the rich and lean premixed reaction zones, particularly in the vicinity of the finite-thickness splitter plates that separate the inner and outer flows (cf. Fig. 1). Flame stabilization can also occur in the very low strain rate region immediately downstream of that plate. In the laboratory, heat transfer will raise the burner surface temperature. Our numerical model considers an isothermal boundary at room temperature, and the computations do not account for the material-dependent heat transfer to the laboratory burner. However, heat transfer is explicitly considered in the predictions through the gas-phase temperature gradient at the inflow boundary, although the boundary temperature in case of the predictions may be lower than that during the experiments.

The heat transfer to the burner Q_b was inferred through thermocouple measurements on a grid (x, y) in the vicinity of the boundary. The measurement grid extended from 0 mm < x < 6 mm (the location $x = 0$ lies along the centerline) and 1 mm < y < 3 mm. The relation

$$Q_b = L^* \Sigma - k(\bar{T})(\Delta T / \Delta y) \, \Delta x, \qquad (2)$$

was used to calculate Q_b, where the summation occurs over the entire transverse burner length L^*, $k(\bar{T})$ denotes the grid-averaged thermal conductivity assuming the mixture to have the properties identical to molecular nitrogen, $\bar{T}$ the mean temperature at two adjacent axial measurement locations, and Δx and Δy (both equal to 0.25 mm) represent the local transverse and axial displacements along the measurement grid. The thermocouple temperatures on the $y = 1$ mm plane lie in the range 440–875 K, and from 500–950 K on the $y = 1.25$ mm plane. Radiation corrections are expected to be insignificant for these temperature values. The thermocouple measurements are not entirely accurate, since the thermocouple is inserted through a nonuniform temperature field [20]. (We have, therefore, used the qualitative holographic measurements for purpose of comparison in Fig. 8.)

This value of the heat transfer was compared to the maximum possible heat release based on the fuel flowrate and its lower heating value. The total heat release for this flame is 1154 W, and the heat transfer to the $(x, y = 1$ mm$)$ plane is 5.9 W. Therefore, we infer that the heat transfer to the burner is $\approx 0.5\%$ of the maximum possible heat release. This ratio is insignificant, even if the combustion efficiency were to fall.

A similar calculation was conducted for the numerical results, although in this case the local conductivity was based on the mixture properties. The heat transfer to the boundary was compared with two values, one based on the heating value of the fuel, and the other on the local heat release rate integrated over the entire computational domain. (The integrated value is lower than that based on the fuel heat release by 12%, primarily because not all of the intermediate species are transformed into CO_2 and H_2O.) The corresponding ratios of heat transfer to the boundary are 0.72% and 0.8%. The lower boundary temperature in case of the computations results in slightly steeper temperature gradients and, consequently, leads to larger gas-phase heat transfer as compared to the experiment.

The heat transfer to the burner or boundary is a negligible proportion of the total heat release in both the computations and the experiments. Furthermore, in both cases the heat transfer to the boundary is of similar magnitude, even though the burner properties are not explicitly modeled. Therefore, we conclude that the presence of the splitter plate in the laboratory burner does not cause a significant anchoring effect due to a flame heat loss mechanism.

Lifted Flames

We were able to obtain lifted flames in the laboratory, but chose to consider one established closer to the burner surface for several reasons. The lifted laboratory flames were not two-dimensional. The wall jets (that we have addressed above) caused the flames to have a bow shape in the cross-stream direction, thereby lifting them higher along the burner sides. A comparison with the numerical simulation requires that the laboratory flame be quasi two-dimensional. In addition, an important objective was to investigate the effects of varying parameters, such as ϕ_{in}, ϕ_{out}, v_{in}, and v_{out}. The flame discussed herein is both more stable and steady over a wide range of conditions, which also precluded an investigation of lifted flames. Unsteady flickering flames are the focus of another investigation in our laboratories [30].

CONCLUSION

An atmospheric laminar methane–air triple flame that is stabilized on a Wolfhard-Parker slot burner has been investigated. A rich mixture is introduced from the inner slot, while a coflowing lean mixture is introduced from the two symmetric outer slots. The three reaction zones that characterize the triple flame have been clearly distinguished. Velocity measurements were made using laser Doppler velocimetry, temperature measurements using laser interferometric holography, and C_2^*-chemiluminescence images that depict the reaction zones and the heat release were obtained. A comprehensive numerical simulation of the flame was performed based on a detailed chemical mechanism involving 24 species and 81 reactions.

The quantitative spatial comparison between spatial locations of the C_2^*-chemiluminescence and the predicted specific heat release rate is excellent. Likewise, the measured and predicted

spatial locations of the three (i.e., triple) reaction zones are virtually identical. In comparison to the other reaction zones the C_2^*-chemiluminescence images do not convey the magnitude of the heat release rate in the lean premixed and nonpremixed reaction zones due to the fact that highly exothermic reactions involving the HO_2 chemistry dominate this zone (rather than the C_2-chemistry from which C_2^* radicals are formed). The comparison between the measured and the predicted velocities is also excellent, which is indicative of the accuracy of the numerical model. There is also excellent qualitative agreement regarding the temperature distribution between holography measurements and numerical predictions, and both sets of results indicate that the inner reaction zone height for a representative flame extends from 18–19 mm.

The effects of the mixture velocity and equivalence ratios on the global triple flame structure have been characterized. As the equivalence ratio in the fuel-rich stream increases or that in the fuel lean stream decreases, the heights of both the inner premixed and the nonpremixed reaction zones increase. In addition, the nonpremixed reaction zone becomes less luminous near its apex and moves closer to the outer lean premixed reaction zone until the two become indistinguishable from each other. A similar effect is observed when the mixture velocities in the two streams are increased. For all the cases investigated, the inner rich premixed zone is found to be stable, whereas both the nonpremixed and the outer lean premixed zones tend to flicker. Only in a few cases is it possible to establish an overall stable triple flame.

The triple flame structure and the interactions between the three reaction zones have been investigated in detail. Methane oxidation to CO_2 and the reduction of molecular oxygen to H_2O follow different pathways in the three reaction zones. The intermediate species CO and H_2 are produced in the inner rich premixed reaction zone. The nonpremixed reaction zone provides radical species that oxidize CO and H_2 to CO_2 and H_2O. Methane consumption is weaker in the outer lean premixed reaction zone, and the concentration of intermediate species, such as CO and H_2, is very small there. Simplifying the chemical mechanism by removing the C_2-containing species produces significant differences in the predicted results only for the inner rich premixed reaction zone.

The heat transfer to the burner or boundary was found to be a negligible proportion of the total heat release in both the computations and the experiments. Therefore, the presence of the splitter plate in the laboratory burner does not appear to cause a significant anchoring effect due to a flame heat loss mechanism.

REFERENCES

1. Ruetsch, G. R., Vervisch, L., and Liñán, A., *Phys. Fluids* 7:1447 (1995).
2. Chung, S. H., and Lee, B. J., *Combust. Flame* 86:62 (1991).
3. Kioni, P. N., Rogg, B., Bray, K. N. C., and Liñán, A., *Combust. Flame* 95:276 (1993).
4. Phillips, H., *Tenth Symposium (International) on Combustion*, Cambridge, 1965, p. 1277.
5. Dold, J. W., *Combust. Flame* 76:71 (1989).
6. Hartley, L. J., and Dold, J. W., *Combust. Sci. Technol.* 80:23 (1991).
7. Dold, J. W., in *Flame Structure*, Nauka Publisher, Novosibirsk, 1991.
8. Muniz, L., and Mungal, M. G., *Combust. Flame* 111:16 (1997).
9. Schefer, R. W., and Goix, P. J., *Combust. Flame* 112:559 (1998).
10. Aggarwal, S. K., and Puri, I. K., *AIAA J.* 36:1190 (1998).
11. Echekki, T., and Chen, J. H., *Combust. Flame* 114:231 (1998).
12. Domingo, P., and Vervisch, L., *Twenty-Sixth Symposium (International) on Combustion*, The Combustion Institute, Pittsburgh, 1996, p. 233.
13. Buckmaster, J., and Matalon, M., *Twenty-Second Symposium (International) on Combustion*, The Combustion Institute, Pittsburgh, 1988, p. 1527.
14. Plessing, T., Terhoeven, P., Peters, N., and Mansour, M. S., *Combust. Flame* 115:335 (1998).
15. Brandon, Y., and Samaniego, J.-M., *Combust. Sci. Technol.* 84:81–89 (1992).

16. McManus, K., Yip, B., and Candel, S., *Exptl. Thermal Fluid Sci*. 10:486–502 (1995).

17. Shu, Z., Krass, B. J., Choi, C. W., Aggarwal, S. K., Katta, V. R., and Puri, I. K., *Twenty-Seventh Symposium (International) on Combustion*, The Combustion Institute, Pittsburgh, 1998, p. 625.

18. Pearse, R. W. B., and Gaydon, A. G., *The Identification of Molecular Spectra*, 4th ed., Chapman and Hall, New York, 1976, p. 83.

19. Najm, H. N., Paul, P. H., Mueller, C. J., and Wyckoff, P. S., *Combust. Flame* 113:312–332 (1998).

20. Xiao, X., Choi, C. W., and Puri, I. K., Paper No. 137, 1999 Joint Meeting of the U.S. Sections of The Combustion Institute, Washington, DC, March 15–17, 1999.

21. Vest, C. M., *Holographic Interferometry*, Wiley, 1979.

22. Montgomery, G. P., and Reuss, D. L., *Appl. Optics* 21:1373 (1982).

23. Hertz, H. M., *Optics Communications* 1:131 (1985).

24. Shu, Z., Aggarwal, S. K., Katta, V. R., and Puri, I. K., *Combust. Flame* 111:276 (1997).

25. Kee, R. J., Miller, J. A., and Warnatz, J. (1983). *A Fortran Program Package for the Evaluation of Gas-Phase Viscosities, Conductivities, and Diffusion Coefficients*, Sandia National Laboratories Rept. SAND83-8209.

26. Peters, N., in *Reduced Kinetic Mechanisms for Applications in Combustion Systems, Lecture Notes in Physics*, *Vol. m15*, (N. Peters and B. Rogg, Eds.), Springer-Verlag, 1993, pp. 3–14.

27. Katta, V. R., Goss, L. P., and Roquemore, W. M., *Combust. Flame* 96:60 (1994).

28. Shu, Z., Choi, C. W., Aggarwal, S. K., Katta, V. R., and Puri, I. K., *Combust. Flame* 118:91–107 (1999).

29. Holman, J. P., *Experimental Methods in Mechanical Engineering*, 6th ed., McGraw-Hill, New York, 1994, p. 49.

30. Azzoni, R., Aggarwal, S. K., and Puri, I. K., Paper No. 167, 1999 Joint Meeting of the U.S. Sections of The Combustion Institute, Washington, DC, March 15–17, 1999.